energies

MDPI

Article

Autonomous Analysis of Infrared Images for Condition Diagnosis of HV Cable Accessories †

Lixiao Mu [1], Xiaobing Xu [2], Zhanran Xia [1], Bin Yang [1], Haoran Guo [1], Wenjun Zhou [2] and Chengke Zhou [2,3,*]

[1] State Grid Hubei Electric Power Company, Wuhan Power Supply Company, Wuhan 430072, China; mulx@hb.sgcc.com.cn (L.M.); xiazr2@hb.sgcc.com.cn (Z.X.); Yangb59@hb.sgcc.com.cn (B.Y.); pengh62@hb.sgcc.com.cn (H.G.)
[2] School of Electrical Engineering and Automation, Wuhan University, Wuhan 430072, China; xuxiaobing@whu.edu.cn (X.X.); wjzhou@whu.edu.cn (W.Z.)
[3] School of Computing, Engineering and Built Environment, Glasgow Caledonian University, Glasgow G4 0BA, UK
* Correspondence: c.zhou@gcu.ac.uk
† This paper is an extended version of our paper published in 2020 IEEE International Conference on High Voltage Engineering and Application (ICHVE), Beijing, China, 6–10 September 2020.

Abstract: Infrared thermography has been used as a key means for the identification of overheating defects in power cable accessories. At present, analysis of thermal imaging pictures relies on human visual inspections, which is time-consuming and laborious and requires engineering expertise. In order to realize intelligent, autonomous recognition of infrared images taken from electrical equipment, previous studies reported preliminary work in preprocessing of infrared images and in the extraction of key feature parameters, which were then used to train neural networks. However, the key features required manual selection, and previous reports showed no practical implementations. In this contribution, an autonomous diagnosis method, which is based on the Faster RCNN network and the Mean-Shift algorithm, is proposed. Firstly, the Faster RCNN network is trained to implement the autonomous identification and positioning of the objects to be diagnosed in the infrared images. Then, the Mean-Shift algorithm is used for image segmentation to extract the area of overheating. Next, the parameters determining the temperature of the overheating parts of cable accessories are calculated, based on which the diagnosis are then made by following the relevant cable condition assessment criteria. Case studies are carried out in the paper, and results show that the cable accessories and their overheating regions can be located and assessed at different camera angles and under various background conditions via the autonomous processing and diagnosis methods proposed in the paper.

Keywords: cable accessories; infrared image processing; Faster RCNN; Mean-Shift algorithm; smart condition diagnosis

Citation: Mu, L.; Xu, X.; Xia, Z.; Yang, B.; Guo, H.; Zhou, W.; Zhou, C. Autonomous Analysis of Infrared Images for Condition Diagnosis of HV Cable Accessories. *Energies* **2021**, *14*, 4316. https://doi.org/10.3390/en14144316

Academic Editors: Issouf Fofana and Bo Zhang

Received: 24 June 2021
Accepted: 14 July 2021
Published: 17 July 2021

1. Introduction

Power cables have been widely used in urban power systems, and their safe operation is key to the reliability of the power grid [1]. Cable accessories, which are used to connect cables with other electrical equipment or different sections of cables, are the weak links of cable systems [2]. Reference [3,4] indicated that the manufacturing of fault-free cable accessories is almost impossible, and poor workmanship during installations and design defects may result in cable faults. Previous studies showed that when there exist defects in cable accessories, such as poor contact of metal connectors, misalignment of stress cones, damage of insulation layer or impurities, and bubbles in the internal medium, the temperature of defective cable accessories was usually higher than those fault free cable accessories [5]. Because the use of infrared thermography to identify abnormal temperatures has many advantages, such as no physical contact, non-intrusive, high

efficiency, and so on, it is widely used in inspection and maintenance activities of power cable circuits [6]. At present, the processing and analysis of infrared images taken during inspections mainly require visual inspection. This is time-consuming and laborious on the one hand, and on the other hand, it relies too much on expert experience and is prone to erroneous diagnosis. Therefore, the realization of autonomous condition diagnosis in cable accessories would greatly benefit the practitioners involved in cable maintenance and inspections.

In previously published researches, the image features related to the temperature gradients of equipment were used as the input of neural networks for the autonomous diagnosis of electrical equipment. In order to analyze the temperature-related information, Rahmani et al. used the Zernike moment as an image feature of fuse bases [7]; Huda et al. extracted the first-order histogram and gray level co-occurrence matrix of infrared images captured from main switchboards [8–10]; Jaffery et al. extracted the RGB color moment of images of fuse cabinets [11]. In the above studies, the key features needed to be selected manually, which was, in fact, a heuristic process. The quality of the selected features was largely dependent on human expertise.

Thus far, there have been few studies on the recognition of infrared images for condition diagnosis of cable accessories. Previously reported research came from the same research team where a number of techniques were investigated for infrared image processing of cable terminations, including the adaptive denoising method based on layer-by-layer optimal basic wavelet and Bayesian estimation [12], the denoising method based on inter-scale correlation of the wavelet coefficients and the bivariate shrinkage function [13], the improved hybrid Fourier-wavelet denoising method [14] and the identification method based on the Radon transform and the Fourier–Mellin transform [15]. Although the above methods were proven to be effective in preliminary image processing, the published work failed to carry out condition diagnosis of real-world infrared images.

This paper proposes a method for autonomous diagnosis of overheating defects in cable accessories based on a Faster RCNN network and Mean-Shift algorithm. Firstly, the collected infrared images of cable accessories during routine inspection activities are used as samples to complete the training of the Faster RCNN network thus as to identify and locate the objects to be diagnosed. Then, the Mean-Shift clustering algorithm is used to segment the images. This helps to extract the overheating area quickly and accurately. Finally, the temperature characteristic parameters are calculated, thus the condition of cable accessories can be diagnosed according to pre-set diagnostic criteria.

2. Object Localization Based on Faster RCNN Network

Cable accessories of interest in this paper include cable terminations and cable grounding boxes. For more information, readers may refer to [16,17]. For the FLIR T630 thermal imager, a handheld camera, which has been applied in work presented in this paper, does not have a specified minimum and maximum shooting distance. When we applied it, the distance between the camera and the target was usually between 1 and 10 m. It was around 1 m when pictures were taken of cable joints and was 3–10 m for cable terminations. As a result, the infrared images under analysis may contain the targeted cable accessories and may also contain other undesired background objects.

The Faster RCNN network, which can identify and locate the desired objects contained in given images, is one of the most advanced algorithms for target detection. Figure 1 shows the flowchart of the Faster RCNN network. Firstly, in order to produce the feature map, it extracts the features of the detected image through a Convolutional Neural Network (CNN). Then, the Region Proposal Network (RPN) is used to propose the possible regions. Next, on the basis of the feature map and proposed regions, the Region of Interest (RoI) pooling layer is applied to extract the proposal feature maps, which are sent to the subsequent network. Finally, the autonomous recognition and positioning of the objects are realized through the object detection layer [18].

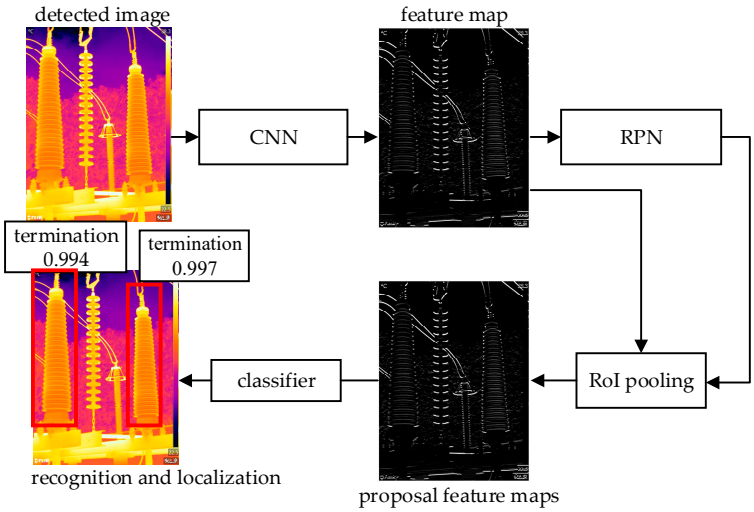

Figure 1. Model of Faster RCNN network.

2.1. Sturcture of Faster RCNN Network

2.1.1. Convolutional Neural Network

Convolutional Neural Network is used to extract feature maps of input images, and the feature maps are shared with the subsequent RPN network and RoI pooling layer. In this paper, the VGG16 Convolutional Neural Network, which includes 13 Convolutional (Conv) layers, 13 Rectified Linear Units (ReLU) layers, and 4 Pooling layers, shown in Figure 2, is adopted.

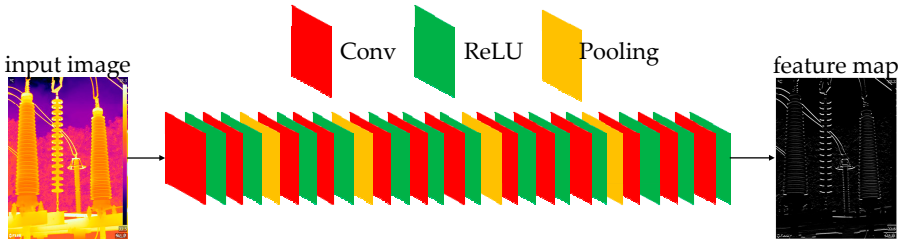

Figure 2. Structure of VGG16 convolutional neural network.

Convolutional layers are applied to detect features of images. It is composed of several convolutional kernels (equivalent to weight matrix k) and additive bias b. Each convolutional kernel can be regarded as a kind of feature detector, which filters the whole image by sliding on the image to capture the corresponding features. From the mathematical point of view, the corresponding features are obtained through the convolutional operation. Suppose the mth layer is a Convolutional layer, then its output vector is as follows:

$$\boldsymbol{x}_j^m = \sum_{\boldsymbol{x}_i \in \boldsymbol{M}_j} \boldsymbol{x}_i^{m-1} * \boldsymbol{k}_{ij}^m + \boldsymbol{b}_j^m \tag{1}$$

where $\boldsymbol{x}_j^m$ is the jth output of this layer; $\boldsymbol{M}_j$ is the set of input vectors; $\boldsymbol{k}_{ij}^m$ is a convolutional kernel; $\boldsymbol{b}_j^m$ is the additive bias, and * represents the convolutional operation.

The size of the output image is as follows:

$$s_{\text{output}} = \frac{s_{\text{input}} - s_{\text{kernel}} + 2 * p}{d} + 1 \tag{2}$$

where s_{output} represents the size of the output image; s_{input} represents the size of the input image; s_{kernel} represents the size of the convolutional kernel; p represents the number of

pixels to be filled, and d represents the step length of the convolutional kernel sliding on the image.

After each convolutional layer, the ReLU layers are applied to enhance the nonlinear characteristics, and the ReLU function is given in (3). Between the Convolutional layers, the Pooling layers are inserted periodically to reduce the dimensionality of features.

$$f(x) = max(0, x) \tag{3}$$

where $f(x)$ stands for the ReLU function, and x represents the characteristic parameters of the output of the convolutional layer.

2.1.2. Region Proposal Network

The Region Proposal Network is used to complete the preliminary positioning of the objects. As is shown in Figure 3, the Region Proposal Network firstly generates a set of rectangular bounding boxes in the detected image. These regions are represented by four-dimensional vectors (x, y, w, h), where x and y denote the region's center coordinates, while w and h denote the width and height. Then, the classification layer is applied to obtain the object score of each proposed region, based on which the Softmax classifier is used to identify the regions that include the diagnostic objects by calculating the probability, using the formula given in (4). On the other hand, to make the positioning more accurate, the regression layer is applied to realize the bounding box regression, based on the formulae given in (5) and (6).

$$P = \frac{e^{z_1}}{e^{z_1} + e^{z_2}} \tag{4}$$

where P represents the probability that the proposed region contains diagnostic objects; z_1 and z_2 represent the foreground score and background score of proposed regions, respectively.

$$\begin{cases} G'_x = A_w d_x(A) + A_x \\ G'_y = A_h d_y(A) + A_y \end{cases} \tag{5}$$

$$\begin{cases} G'_w = A_w \exp(d_w(A)) \\ G'_h = A_h \exp(d_h(A)) \end{cases} \tag{6}$$

where (A_x, A_y, A_w, A_h) denote the unadjusted coordinates of the bounding box. (G'_x, G'_y, G'_w, G'_h) denote the adjusted coordinates. $d_x(A)$ and $d_y(A)$ denote the translation parameters, $d_w(A)$ and $d_h(A)$ denote the scale parameters.

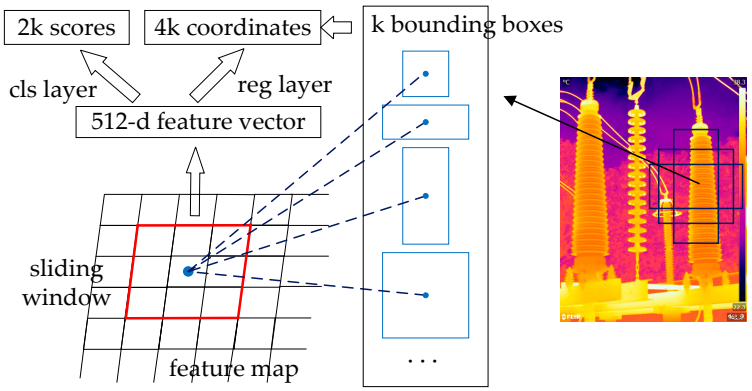

Figure 3. Structure of RPN network.

2.1.3. Region of Interest Pooling Layer

The RoI Pooling layer can obtain the fixed-length feature vectors by analyzing input data of different sizes. The operating principle is shown in Figure 4. Assuming that the size of input feature map is 8×8, and the box calibration region is the proposed feature.

According to the transformation factors p_w and p_h, the proposed feature is divided into $p_w \times p_h$ blocks ($p_w = p_h = 2$ in this example). Then the maximum pooling is applied for each block in order to the maximum value of each block.

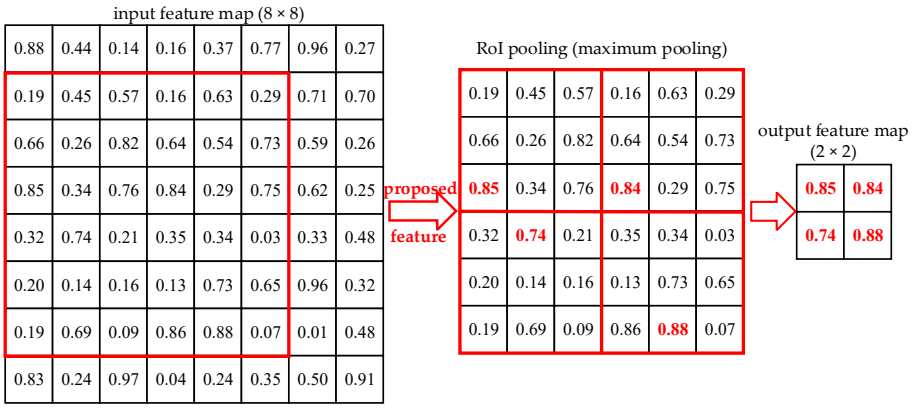

Figure 4. Operating principle of RoI pooling layer.

In the Faster RCNN network, the pooling process of the RoI Pooling layer is shown in Figure 5. Firstly, the regions proposed by the RPN are mapped to the feature map obtained by the CNN, to allow the proposal feature maps of different sizes to be extracted. Next, according to p_w and p_h ($p_w = p_h = 7$ in this paper), maximum pooling is applied to convert the proposal features into feature maps with the fixed spatial extent of 7×7. Finally, the fixed-length proposal feature maps are sent to the subsequent network.

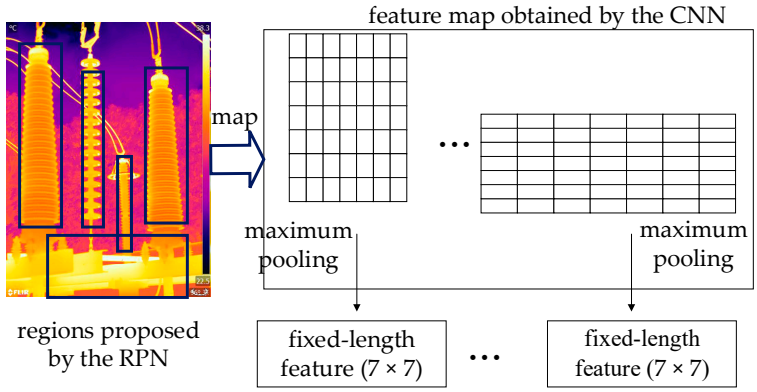

Figure 5. Pooling process of RoI pooling layer.

2.1.4. Object Detection Layer

As is shown in Figure 6, based on the proposal feature maps, the Softmax classifier is used to achieve object identification (objects to be identified include cable terminations and grounding boxes in this paper). On the other hand, the regression layer is applied to complete the second bounding box regression, which makes the localization more precise.

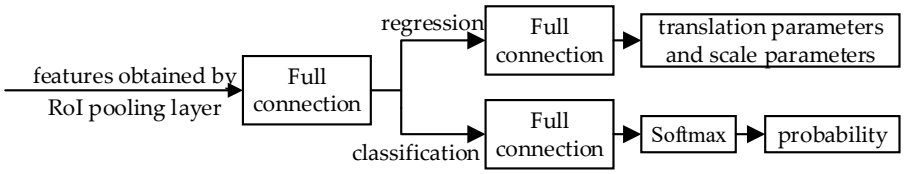

Figure 6. Operating principle of object detection layer.

2.2. Autonomous Detection Results of Faster RCNN Network

The infrared images captured by the infrared thermal imagers (FLIR T630) were used as samples to train the Faster RCNN network. Table 1 shows the specifications of the FLIR T630 handheld thermal cameras. When the infrared images of power cable accessories were taken, the emissivity coefficients of imagers were set to 0.9.

Table 1. Specifications of the FLIR T630 handheld thermal cameras.

Specifications	
Detector resolution	640 × 480
Accuracy	±2 °C or ±2% of reading
Thermal sensitivity	<30 mK @ 30 °C
Operating temperature range	−15 °C to 50 °C
Operating humidity	95% relative humidity
Object temperature range	−40 °C to 650 °C
Atmosphere transmission correction	automatic
External optics and widows correction	automatic
Optics transmission correction	automatic
Reflected apparent temperature correction	automatic

The abnormal heating phenomenon usually occurs at connection fittings and sleeves of the cable terminations or the connections of the grounding boxes. Therefore, when constructing the training samples, if the diagnostic objects are the terminations, the labeled target should be the connection fittings and sleeves. If the objects under analysis are grounding boxes, the marked target should be the connections. After completing the training, the Faster RCNN network can realize the autonomous identification and positioning of the cable terminations and grounding boxes in images.

Taking Figures 7 and 8 as examples, where Figures 7a and 8a, respectively, show the original infrared images of grounding box and cable termination taken during routine inspection activities. Figures 7b and 8b show the recognition and positioning results of the trained Faster RCNN network. To eliminate the influence of the interference information, the image contents inside the proposal regions were kept, while other contents were eliminated by setting the pixels' components of red (R), green (G), and blue (B) to zero. The extracted connections of the grounding box are shown in Figure 7c. The extracted connection fitting is shown in Figure 8c, and the extracted sleeve in Figure 8d. The results show that based on the Faster RCNN network, the diagnostic objects were accurately extracted, and the interference of complex background and foreground, which my hamper subsequent image processing, were eliminated.

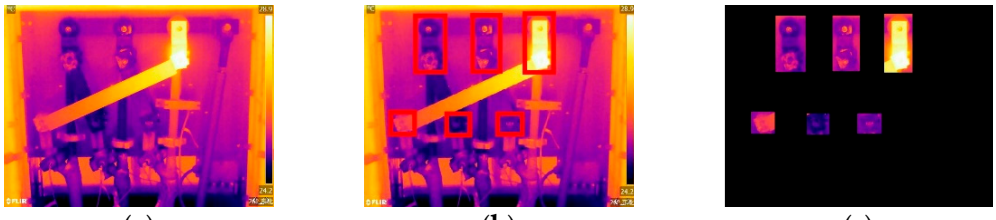

(**a**) (**b**) (**c**)

Figure 7. Result of eliminating the interference information in the image of the grounding box: (**a**) original infrared image; (**b**) detecting result of Faster RCNN network; (**c**) extracting results of connections.

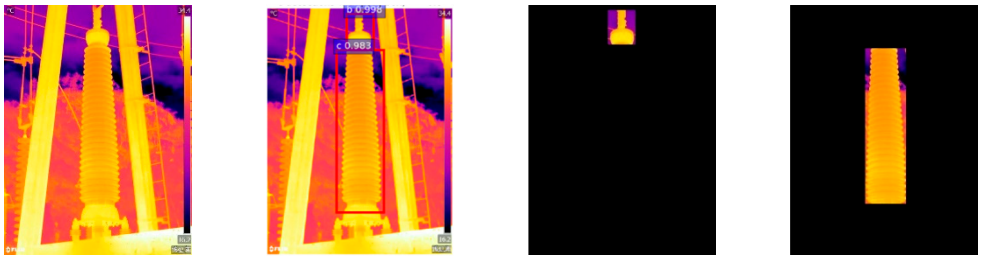

(**a**) (**b**) (**c**) (**d**)

Figure 8. Results of eliminating the interference information in the image of termination: (**a**) original infrared image; (**b**) detecting results of Faster RCNN network; (**c**) extracting result of the connection fitting; (**d**) extracting result of the sleeve.

3. Extraction of Suspected Abnormal Heating Regions Based on Mean-Shift Algorithm

After extracting the diagnostic objects, it is necessary to extract the suspected abnormal heating regions among the objects. In subsequent processing, their temperature distribution is the basis for condition diagnosis.

The gray information of the infrared images reflects the temperature distribution. The greater the gray value of the pixel, the higher the corresponding temperature. Therefore, the gray value is to be extracted from the infrared images. The graying formula is as follows [19]:

$$I = 0.299R + 0.587G + 0.114B \tag{7}$$

where, I is the gray value of the pixel; R is the red component; G is the green component, and B is the blue component.

The Mean-Shift algorithm, which has been widely used in clustering, is essentially an iterative search algorithm [20]. In this paper, the gray values of pixels were used as the data samples, and the Mean-Shift algorithm was applied to cluster the pixels. The clustering process is shown in Figure 9. Firstly, a pixel was randomly selected to be the clustering center, and other pixels, of which the grayscale difference with the center less than the bandwidth, were placed in the same class. The bandwidth h_r realized adaptive selection based on the asymptotic mean integrated square error (AMISE) is as shown in (8) and (9) [21]. Then, the Mean-Shift vector was calculated, and the original center moved the vector to obtain the new center [22]. The clustering center was updated until the convergence condition was satisfied. The above steps were repeated until all the pixels were traversed.

$$h_r = \left(\frac{4}{d+2}\right)^{1/(d+4)} n^{-1/(d+4)}\sigma \tag{8}$$

$$\sigma = \sqrt{\frac{1}{n-1}\sum_{i=1}^{n}(x_i - \overline{x})^2} \tag{9}$$

where, h_r represents the bandwidth; d the dimension of the feature space; n the number of samples; σ the standard deviation; x the sample, and $\overline{x}$ represents the average value of the sample data.

In order to describe the Mean-Shift clustering process more intuitively, this paper takes the cable grounding box as an example, as is shown in Figure 10. Figure 10a shows the result of autonomous positioning and identification of the diagnostic objects (connections) in infrared images by trained Faster RCNN network. Figure 10b shows the corresponding grayscale image. Figure 10c shows the three-dimensional visualization result of the pixels' gray information, where each scatter point corresponds to a pixel in the image, (x, y) represents the position information of the corresponding pixel in the original image, and z represents the gray value of the pixel. Figure 10d shows the result of clustering by the

Mean-Shift algorithm. In order to reflect the clustering result more intuitively, the pixels belonging to the same category were marked with the same color.

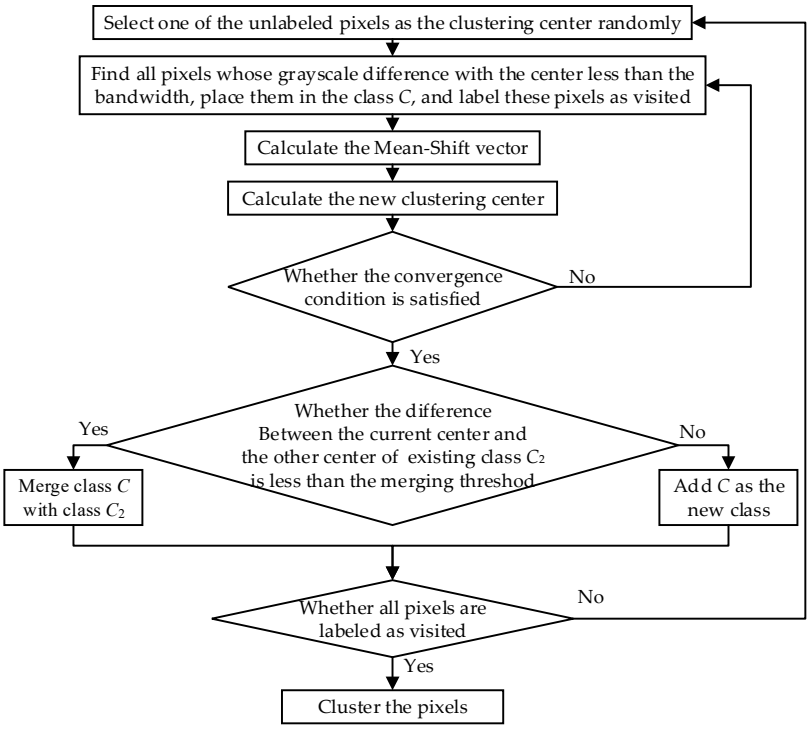

Figure 9. Clustering process of Mean-Shift algorithm.

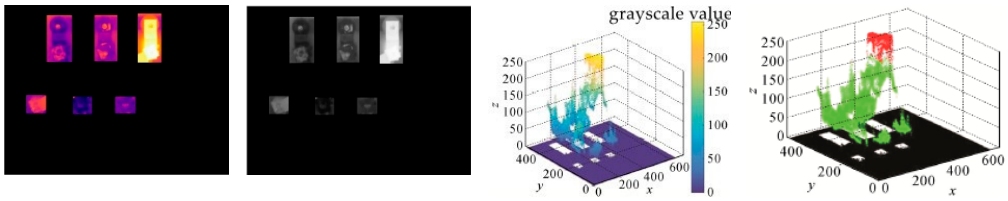

Figure 10. Clustering result of Mean-Shift algorithm: (**a**) detecting results of Faster RCNN network; (**b**) grayscale image; (**c**) three-dimensional visualization result of the pixel gray information; (**d**) clustering result.

As can be seen in Figure 10d, the pixels in the example were adaptively divided into three categories. The pixels marked in black correspond to the background area in the original image. The pixels marked in green correspond to the regions under normal conditions, and the pixels marked in red correspond to the suspected overheating regions. Therefore, after clustering based on the Mean-Shift algorithm, this paper retained the category with the center, where the gray value was the greatest, as the suspected overheating area.

Taking the infrared images of the HV cable accessories captured during an inspection as the testing objects. In order to achieve the best results, after realizing the autonomous identification and positioning of the diagnostic objects, this paper, respectively, applied the Maximum Between-Class Variance (OTSU) algorithm, the K-Means algorithm, and the Mean-Shift algorithm to segment the images. The OTSU algorithm can adaptively calculate the segmentation threshold, and the pixels of which the gray values are lower than the threshold were categorized into the background, while other pixels, of which the gray values are higher than the threshold, were categorized into the foreground [23]. The K-Means algorithm randomly selected k pixels as clustering centers according to the given k, and then classified the remaining pixels to the most similar center before it updated the

clustering centers to the mean value of each category. The above steps were repeated until the convergence condition is satisfied [24,25].

Based on the clustering results, the suspected abnormal heating regions were extracted, as is shown in Figure 11. Figure 11a shows the original infrared images of grounding box I, grounding box II, termination I, and termination II. Figure 11b shows the detecting results of diagnostic objects by the Faster RCNN network. Figure 11c, Figure 11d,e show the extracting results of suspected abnormal heating regions by different clustering algorithms.

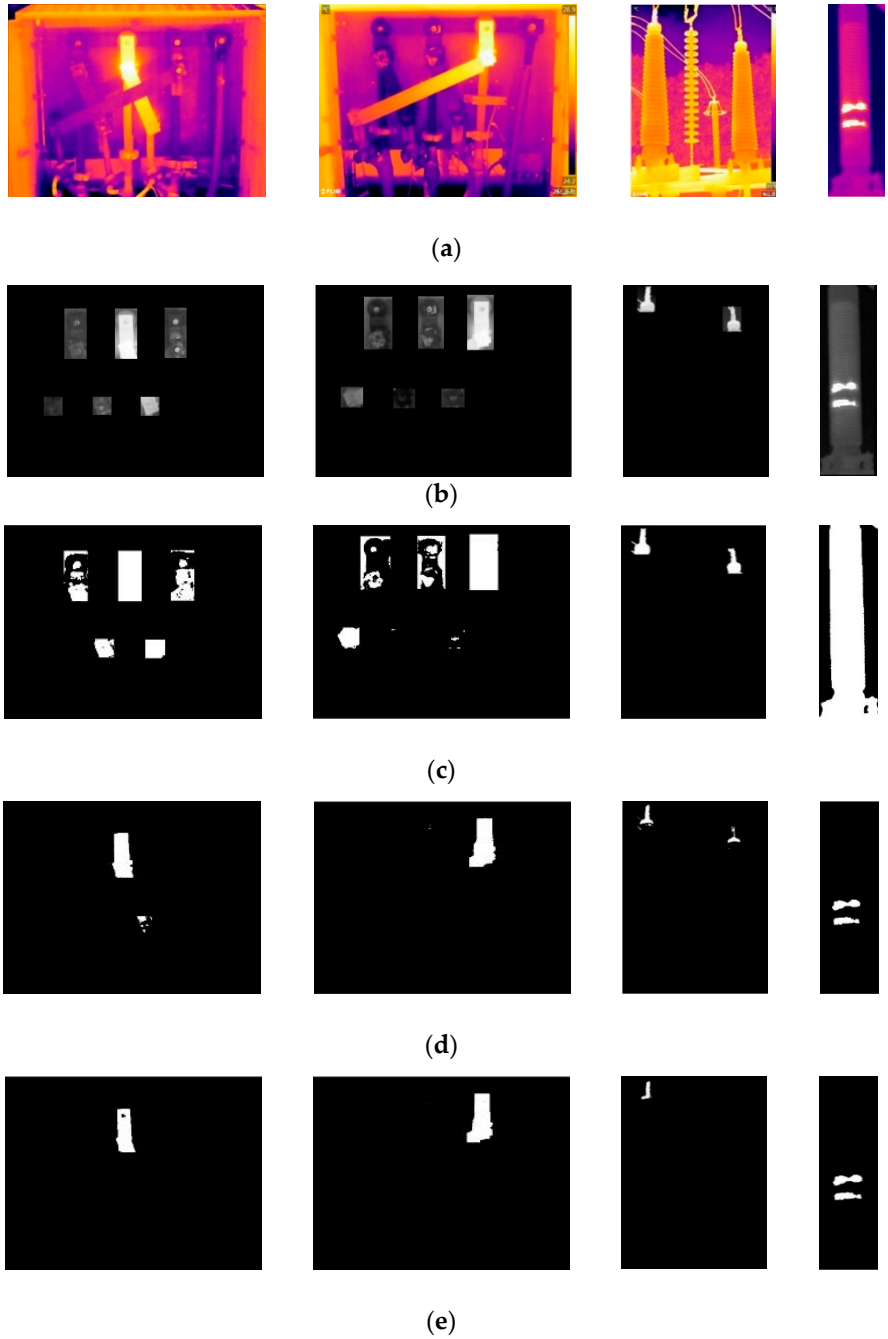

Figure 11. Results of extracting the suspected abnormal heating regions: (**a**) original infrared images, (**b**) detecting results of diagnostic objects by Faster RCNN network, (**c**) extracting results of the OTSU algorithm, (**d**) extracting results of the K-Means algorithm, (**e**) extracting results of the Mean-Shift algorithm.

As shown in Figure 11, the adaptive segmentation threshold calculated by the OTSU algorithm was often too low to distinguish the abnormal heating regions from the area under normal conditions. Thus, in the final segmentation results, the abnormal heating area was almost submerged in the diagnostic objects. The K-Means algorithm can specify the number of categories manually, which solves the disadvantage of the OTSU algorithm that it can only achieve dichotomy. Therefore, compared with the OTSU algorithm, the clustering results by K-Means algorithm represented an improvement. However, for different images, the most suitable number of clustering categories is also different. Thus, some regions under normal conditions were still identified as abnormal heating regions wrongly by the K-Means algorithm. The Mean-Shift algorithm can adaptively select the most appropriate number of clustering categories according to the gray information of the image, which can overcome the disadvantage of the K-Means algorithm. The testing results showed that the Mean-Shift algorithm could extract the abnormal heating regions accurately, and its performance was better than the OTSU algorithm and the K-Means algorithm.

4. Positioning of Reference Regions

In order to accurately realize condition diagnosis after extracting the abnormal heating regions, the reference regions should be localized in the reference phases, which do not have abnormal heating regions (assuming that at least one phase is in normal status in this paper). This article applied different methods to locate the positions of reference regions for different HV cable accessories.

4.1. Grounding Boxes

If the diagnostic object was a grounding box, the Faster RCNN network would have directly positioned the connections (including the upper side connections and the lower side connections). The phase (one of the three phases), which contained the overheating area, was noted as the suspected overheating phase, and the remaining phases, which always had the same height, were regarded as the reference phases. The whole reference phases can be deemed as the reference regions.

Figure 12 shows the positioning results of reference regions of the grounding boxes. To describe the positioning process more intuitively, the four-dimensional vectors (x_1, y_1, x_2, y_2) were used to represent the position of each phase, where x_1 and x_2 denote the horizontal coordinates of top-left corner and bottom-right corner of each phase, while y_1 and y_2 denote the vertical coordinates. The position information of the suspected overheating phase of the grounding box I was (268, 65, 339, 184), while the position information of other phases was (148, 65, 219, 184), (390, 65, 461, 184), (100, 290, 142, 338), (214, 290, 256, 338), and (339, 290, 381, 338). Thus, the connections corresponding to the first two data sets were regarded as the reference regions because they had the same vertical coordinates with the overheating phase. The positioning method of reference regions of grounding box II was the same.

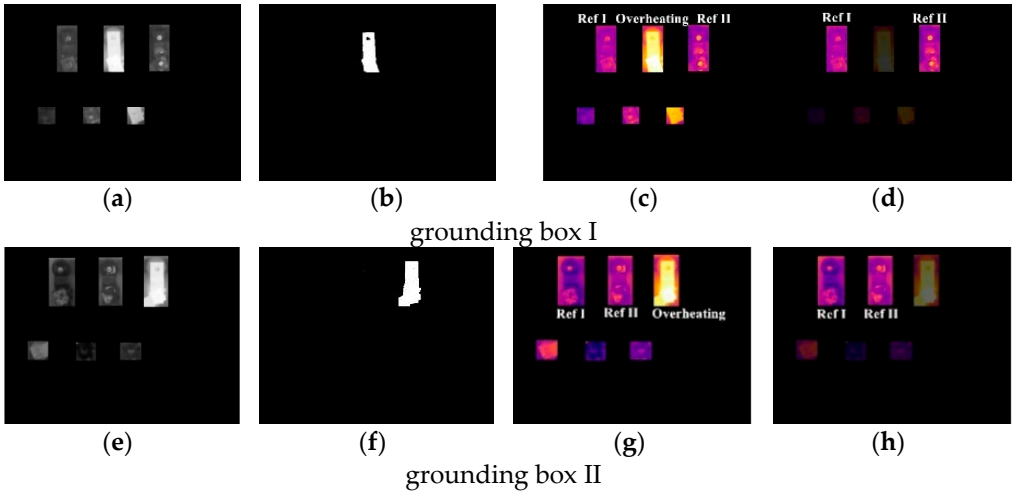

Figure 12. Reference regions locating results of grounding boxes: (**a**,**e**) grayscale image, (**b**,**f**) extracting results of suspected overheating regions, (**c**,**g**) suspected overheating phase and reference phases, (**d**,**h**) locating results of reference regions.

4.2. Cable Terminations

When the object to be diagnosed was a cable termination, the Faster RCNN network was firstly applied to locate the connection fittings and sleeves. The phase that included abnormal heating regions were regarded as the suspected abnormal heating phase, and the remaining phases were considered as the reference phases. Considering the similarity of the structure among the three phases of the termination, the reference regions can be positioned according to the abnormal heating area's position information and the size ratio of different phases of terminations identified in the image. Taking Figure 13 as an example, (10) and (11) were used to calculate the coordinate information of the reference regions' pixels. The highlighted areas in Figure 13d,h show the positioning results of reference regions.

$$\begin{cases} \boldsymbol{X}_{\text{hot}} = [x_1, x_2, x_3, \ldots, x_n] \\ \boldsymbol{Y}_{\text{hot}} = [y_1, y_2, y_3, \ldots, y_n] \end{cases} \tag{10}$$

$$\begin{cases} \boldsymbol{X}_{\text{ref}} = (\boldsymbol{X}_{\text{hot}} - x_{\text{min1}})/(x_{\text{max1}} - x_{\text{min1}}) * (x_{\text{max2}} - x_{\text{min2}}) + x_{\text{min2}} \\ \boldsymbol{Y}_{\text{ref}} = (\boldsymbol{Y}_{\text{hot}} - \text{y}_{\text{min1}})/(\text{y}_{\text{max1}} - \text{y}_{\text{min1}}) * (\text{y}_{\text{max2}} - \text{y}_{\text{min2}}) + \text{y}_{\text{min2}} \end{cases} \tag{11}$$

where $\boldsymbol{X}_{\text{hot}}$ and $\boldsymbol{Y}_{\text{hot}}$, respectively, denote the horizontal coordinates and vertical coordinates of the abnormal heating regions' pixels; $\boldsymbol{X}_{\text{ref}}$ and $\boldsymbol{Y}_{\text{ref}}$, respectively, denote the horizontal coordinates and vertical coordinates of the reference regions' pixels. n denotes the number of pixels in the abnormal heating regions; (x_{min1}, x_{max1}) and (y_{min1}, y_{max1}) the horizontal coordinates and vertical coordinates of the top-left corner and bottom-right corner of the suspected abnormal heating phase. (x_{min2}, x_{max2}) and (y_{min2}, y_{max2}) the vertical coordinates of the top-left corner and bottom-right corner of the reference phase.

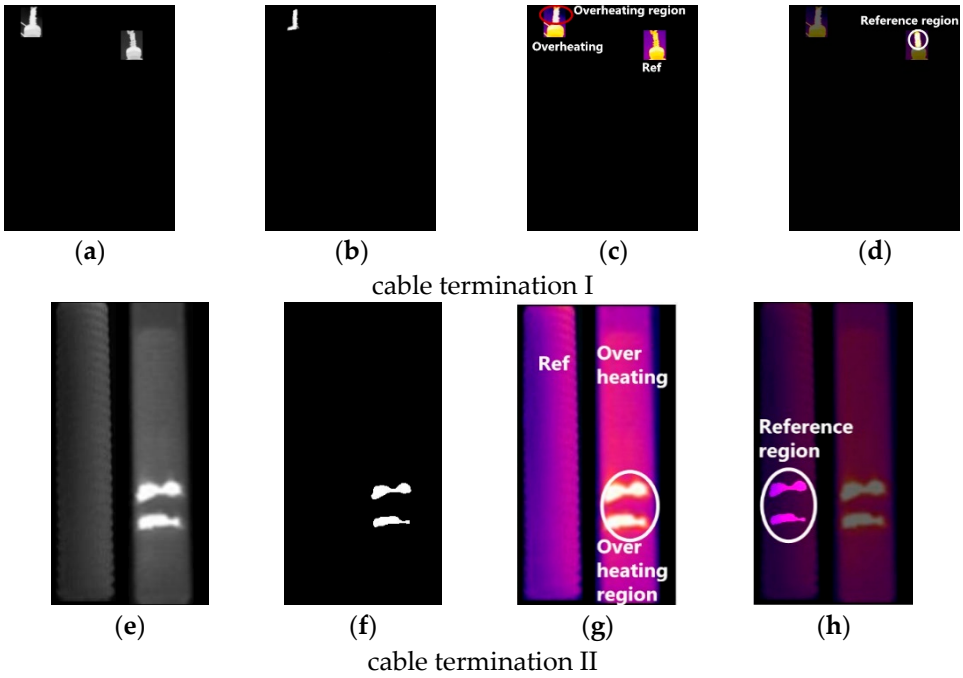

Figure 13. Location results of reference regions of cable terminations: (**a**,**e**) grayscale image, (**b**,**f**) extracting results of suspected abnormal heating regions, (**c**,**g**) suspected abnormal heating phase and reference phases, (**d**,**h**) locating results of reference regions.

5. Calculation of Temperature Parameters and Condition Diagnosis

In order to diagnose the severity of the overheating defect, T_1 and T_2, which denote the maximum temperature of the identified abnormal heating area and reference area, respectively, were extracted. Combined with the ambient temperature T_0, the temperature characteristic parameters can be calculated according to (12)~(14).

$$T_r = T_1 - T_0 \tag{12}$$

$$T_d = T_1 - T_2 \tag{13}$$

$$\delta = (T_1 - T_2)/(T_1 - T_0) \tag{14}$$

where T_r is the value of temperature rise; T_d is the value of temperature difference, and δ represents the value of relative temperature difference.

According to the corresponding diagnostic criteria, the autonomous diagnosis of overheating defects in cable accessories can be achieved based on the calculated temperature characteristic parameters. Table 2 shows the diagnostic criteria from the "Guidelines for defective grading standards of power transmission equipment of Guangdong Power Grid Company (version 2018)". Table 3 shows the calculated temperature parameters and diagnosis results of Figures 12 and 13. The temperature difference of grounding box I in Figure 12 was 6.4 °C. Because it was between 5 °C and 15 °C, the status of grounding box I was regarded as the general defect. The temperature difference of grounding box II was only 2.9 °C, which was lower than 5 °C. In addition, the temperature rise was only 4.6 °C, which was less than 15 °C, the condition of grounding box II was diagnosed to be normal. Similarly, the temperature difference of connection fittings of cable terminations I in Figure 13 was 50.6 °C, which was higher than 40 °C, thus the termination I was judged to have a defect needing urgent action. The temperature difference of sleeves of cable terminations II was 11.2 °C, thus the condition of this termination was determined as having a major defect.

Table 2. Diagnostic standard for HV cable accessories.

Defective Part	Defective Appearance	Severity Level
Connection fittings of cable terminations or connections of grounding boxes	Temperature of heating spot >130 °C; Temperature difference >40 °C; Relative temperature difference >95% and temperature rise >15 °C	Urgent
	Temperature of heating spot: 90~130 °C; Temperature difference: 15~40 °C; Relative temperature difference: 80%~95% and temperature rise >15 °C	Major
	Temperature difference: 5~15 °C; Relative temperature difference: 35%~80% and temperature rise >15 °C	General
sleeves of cable terminations	Temperature difference >4 °C	Major
	Temperature difference: 2~4 °C	General

Table 3. Temperature calculation and diagnostic results of cable accessories.

Cable Accessories	Temperature/°C				T_r[1]/°C	Max T_d[2]/°C	Max σ[3]/%	Diagnostic Results
	Heating	Ref I	Ref II	Environment				
Grounding box I	31.4	25	26.4	23	8.4	6.4	76.2	General defect
Grounding box II	29.6	26.7	27.1	25	4.6	2.9	63	Normal
Termination I	86.3	35.7	\	32	54.3	50.6	93.18	Urgent defect
Termination II	47.3	36.1	\	22	25.3	11.2	44.27	Major defect

[1] T_r means the temperature rise, [2] max T_d means the maximum temperature difference, [3] max σ means the maximum relative temperature difference.

The proposed method has been applied to test against actual infrared images, including 50 images of cable terminations and 50 images of grounding boxes. The testing results are shown in Table 4.

Table 4. Testing results of inspection images.

Cable Accessories	Actual Condition		Autonomous Diagnosis Results	
Cable terminations	Normal	32	Normal	32
	General defect	2	General defect	2
	Major defect	7	Major defect	7
	Urgent defect	9	Urgent defect	9
Grounding boxes	Normal	40	Normal	39
	General defect	7	General defect	8
	Major defect	1	Major defect	1
	Urgent defect	2	Urgent defect	2

6. Conclusions

This paper is an extension of a conference paper, which the authors previously published [25]. It proposed an autonomous method to analyze infrared images for the diagnosis of insulation conditions of cable accessories. The approach included the positioning and identification of diagnostic objects, the extraction of key regions, and the calculation of temperature parameters for condition assessment of cable accessories. The conclusions are as follows:

(1) The method for autonomous positioning and identification of cable accessories in infrared images based on Faster RCNN network was proposed. This method was applied to test against actual infrared images, and results showed that the autonomous location and

recognition could be achieved at different shooting angles and under various background conditions.

(2) The method for extracting suspected abnormal heating regions based on Mean-Shift algorithm was proposed. Case studies showed that this method, which was superior to other alternatives, can realize image adaptive segmentation. It can extract the abnormal heating regions of grounding boxes and cable terminations accurately.

(3) The proposed method may potentially be productive as it helps reduce the dependence on human efforts and expertise and helps improve the practice of intelligent condition monitoring.

Author Contributions: Conceptualization, L.M., Z.X., C.Z., X.X.; methodology, L.M., Z.X., C.Z., W.Z.; software, B.Y., H.G.; validation, L.M., Z.X., C.Z., W.Z.; formal analysis, L.M., Z.X., C.Z., X.X.; investigation, L.M., Z.X., C.Z., X.X.; resources, B.Y., H.G.; data curation, B.Y., H.G.; writing—original draft preparation, X.X., L.M., Z.X.; writing—review and editing, C.Z., W.Z.; visualization, X.X., L.M., Z.X.; supervision, L.M., Z.X., C.Z., W.Z.; project administration, L.M., Z.X., C.Z., W.Z.; funding acquisition, L.M., Z.X., B.Y., H.G. All authors have read and agreed to the published version of the manuscript.

Funding: This research was funded by Science and Technology Project of State Grid Hubei Electric Power Company, grant number SGHBWH00YJJS2001955.

Institutional Review Board Statement: Non applicable.

Informed Consent Statement: Non applicable.

Data Availability Statement: Non applicable.

Conflicts of Interest: The authors declare no conflict of interest.

References

1. Lowczowski, K.; Lorenc, J.; Tomczewski, A.; Nadolny, Z.; Zawodniak, J. Monitoring of MV cable screens, cable joints and earthing systems using cable screen current measurements. *Energies* **2020**, *13*, 3438. [CrossRef]
2. Zhou, L.J.; Zhu, S.B.; Bai, L.L.; Liu, Y.; Zhu, L.; Guo, L. Influence of stress tubes interface on partial discharge of vehicle cable terminal at low temperatures. *High Voltage Eng.* **2019**, *45*, 1266–1273.
3. Reda, A.M.; Al-Yafei, A.M.S.; Howard, I.M.; Forbes, G.L.; McKee, K.K. Simulated in-line deployment of offshore rigid field joint—A testing concept. *Ocean Eng.* **2016**, *112*, 153–172. [CrossRef]
4. Reda, A.; Abu-Siada, A.; Howard, I.M.; McKee, K.K. A testing platform for subsea power cable deployment. *Eng. Fail. Anal.* **2019**, *96*, 142–157. [CrossRef]
5. Xiong, L.; Chen, Y.H.; Jiao, Y.; Wang, J.; Hu, X. Study on the effect of cable group laying mode on temperature field distribution and cable ampacity. *Energies* **2019**, *12*, 3397. [CrossRef]
6. Ullah, I.; Khan, R.U.; Yang, F.; Wuttisittikulkij, L. Deep learning image-based defect detection in high voltage electrical equipment. *Energies* **2020**, *13*, 392. [CrossRef]
7. Rahmani, A.; Haddadnia, J.; Seryasat, O.L. Intelligent fault detection of electrical equipment in ground substations using thermos vision technique. In Proceedings of the 2010 2nd International Asia Conference on Mechanical and Electronics Engineering (ICMEE), Kyoto, Japan, 1–3 August 2010.
8. Huda, A.S.N.; Taib, S.; Jadin, M.S.; Ishak, D. A semi-automatic approach for thermographic inspection of electrical installations within buildings. *Energy Build* **2012**, *55*, 585–591. [CrossRef]
9. Huda, A.S.N.; Taib, S.; Ghazali, K.H.; Jadin, M.S. A new thermographic NDT for condition monitoring of electrical components using ANN with confidence level analysis. *ISA Trans.* **2014**, *53*, 717–724. [CrossRef]
10. Ullah, I.; Yang, F.; Khan, R.; Liu, L.; Yang, H.S.; Gao, B.; Sun, K. Predictive maintenance of power substation equipment by infrared thermography using a machine-learning approach. *Energies* **2017**, *10*, 1987. [CrossRef]
11. Jaffery, Z.A.; Dubey, A.K. Design of early fault detection technique for electrical assets using infrared thermograms. *Int. J. Electr. Power Energy Syst.* **2014**, *63*, 753–759.
12. Wu, J.Z.; Niu, H.Q.; Xu, J. Adaptive de-noising method for infrared image of porcelain bushing cable terminal based on layer optimal basic wavelet and Bayes estimation. *Electr. Meas. Instrum.* **2016**, *53*, 83–89.
13. Niu, H.Q.; Wu, J.Z.; Xu, J.; Wu, Q.; Gao, Z.J.; Zheng, W.J. Denoising of infrared images of porcelain sleeve cable terminal considering inter-scale correlation. *J. South China Univ. Technol. (Natl. Sci. Ed.)* **2017**, *45*, 15–21.
14. Wu, J.Z.; Niu, H.Q.; Zhang, H.; Xu, J. A hybrid Fourier-wavelet de-noising method for infrared image of porcelain sleeve cable terminal using GSM model for wavelet coefficients. *Electr. Meas. Instrum.* **2018**, *55*, 113–117.
15. Niu, H.Q.; Wu, J.Z.; Xu, J.; Zheng, W.Q. Infrared image recognition of cable terminal based on Randon and Fourier-Mellin Transform. *J. South China Univ. Technol. (Natl. Sci. Ed.)* **2016**, *44*, 47–52.

16. Wan, L.; Zhou, K.; Li, X.T.; Wu, K. Toward understanding development mechanism of partial discharge in air gap defects in cable termination by analysis of electric field characteristics. *High Voltage Eng.* **2014**, *40*, 3709–3716.
17. Yang, J.; Zhu, X.L.; Dong, X.; Lu, Y.; Li, N. On-line monitoring and diagnosis of HV cable faults based on sheath currents. *High Voltage Eng.* **2016**, *42*, 3616–3625.
18. Ren, S.Q.; He, K.M.; Girshick, R.; Sun, J. Faster R-CNN: towards real-time object detection with region proposal networks. In Proceedings of the 2016 Conference and Workshop on Neural Information Processing Systems (NIPS), Barcelona, Spain, 9–10 December 2016.
19. Yang, Y. Infrared image analysis and processing of power equipments. Master's Thesis, Beijing Jiaotong University, Beijing, China, 2015.
20. Kim, N.; Park, S.; Lee, J.; Choi, J.K. Load profile extraction by Mean-Shift clustering with Sample Pearson Correlation Coefficient distance. *Energies* **2018**, *11*, 2397. [CrossRef]
21. Hong, Y.P.; Yi, J.Q.; Zhao, D.B. Improved mean shift segmentation approach for natural images. *Appl. Math. Comput.* **2007**, *185*, 940–952. [CrossRef]
22. Zhou, Z.Q.; Feng, Z.X.; Zhou, D.G.; Xu, X.L.; Gu, K.K. Fault region extraction of electrical equipment in infrared image by using an extended Mean Shift method. *Infrared Technol.* **2019**, *41*, 78–83.
23. Otsu, N. A threshold selection method from gray-level histograms. *IEEE Trans. Syst. Man Cybern.* **1979**, *9*, 62–66. [CrossRef]
24. Zhang, Y.J.; Yang, L.F.; Ge, S.Y.; Zhou, H.X. Short-term photovoltaic power forecasting based on Kmeans algorithm and support vector machine. *Power Syst. Prot. Control* **2018**, *46*, 118–124.
25. Xu, X.B.; Zhou, C.K.; Zhou, W.J.; Liao, Y.Q.; Wei, Y.L.; Yuan, J. Autonomous diagnosis of overheating defects in cable accessories based on Faster RCNN and Mean-Shift algorithm. In Proceedings of the 2020 IEEE International Conference on High Voltage Engineering (ICHVE 2020), Beijing, China, 6–10 September 2020.